PHYSICAL REVIEW B **111**, 014421 (2025)

Magnetic properties of a staggered S= 1 chain with an alternating single-ion anisotropy direction

S. Vaidya,[1,2,*] S. P. M. Curley,[1] P. Manuel,[3] J. Ross Stewart,[3] M. Duc Le,[3] C. Balz,[3,4] T. Shiroka,[5,6] S. J. Blundell,[7] K. A. Wheeler,[8] I. Calderon-Lin,[9] Z. E. Manson,[9] J. L. Manson,[9,†] J. Singleton,[10] T. Lancaster,[11] R. D. Johnson,[12,13] and P. A. Goddard[1,‡]

[1]*Department of Physics, University of Warwick, Gibbet Hill Road, Coventry CV4 7AL, United Kingdom*
[2]*School of Physics & Astronomy, University of Birmingham, Edgbaston, Birmingham B15 2TT, United Kingdom*
[3]*ISIS Pulsed Neutron Source, STFC Rutherford Appleton Laboratory, Didcot, Oxfordshire OX11 0QX, United Kingdom*
[4]*Neutron Scattering Division, Oak Ridge National Laboratory, Oak Ridge, Tennessee 37831, USA*
[5]*PSI Center for Neutron and Muon Sciences CNM, Forschungsstrasse 111, 5232 Villigen PSI, Switzerland*
[6]*Laboratorium für Festkörperphysik, Otto-Stern-Weg 1, ETH Zürich, CH-8093 Zurich, Switzerland*
[7]*Department of Physics, Clarendon Laboratory, University of Oxford, Parks Road, Oxford OX1 3PU, United Kingdom*
[8]*Department of Chemistry, Whitworth University, Spokane, Washington 99251, USA*
[9]*Department of Chemistry and Biochemistry, Eastern Washington University, Cheney, Washington 99004, USA*
[10]*National High Magnetic Field Laboratory (NHMFL), Los Alamos National Laboratory, Los Alamos, New Mexico 87545, USA*
[11]*Department of Physics, Durham University, Durham DH1 3LE, United Kingdom*
[12]*Department of Physics and Astronomy, University College London, Gower Street, London WC1E 6BT, United Kingdom*
[13]*London Centre for Nanotechnology, University College London, London WC1H 0AH, United Kingdom*

(Received 25 July 2024; accepted 4 December 2024; published 17 January 2025; corrected 11 April 2025 and 29 April 2025)

Materials composed of spin-1 antiferromagnetic (AFM) chains are known to adopt complex ground states that are sensitive to the single-ion-anisotropy (SIA) energy (D), and intrachain (J_0) and interchain ($J'_{1,2}$) exchange energy scales. While theoretical and experimental studies have extended this model to include various other energy scales, the effect of the lack of a common SIA axis is not well explored. Here we investigate the magnetic properties of Ni(pyrimidine)$(H_2O)_2(NO_3)_2$, a chain compound where the tilting of Ni octahedra leads to a twofold alternation of the easy-axis directions along the chain. Muon-spin relaxation measurements indicate a transition to long-range order at T_N = 2.3K and the magnetic structure is initially determined to be antiferromagnetic and collinear using elastic neutron diffraction experiments. Inelastic neutron scattering measurements were used to find J_0 = 5.107(7)K, $D = 2.79(1)$ K, $J'_1 = 0.00(5)$K, $J'_2 = 0.18(3)$K, and a rhombic anisotropy energy

E = 0.19(9)K. Mean-field modeling reveals that the ground state structure hosts spin canting of $\phi \approx 6.5^\circ$, which is not detectable above the noise floor of the elastic neutron diffraction data. Monte Carlo simulation of the powder-averaged magnetization, $M(H)$, is then used to confirm these Hamiltonian parameters, while single-crystal $M(H)$ simulations provide insight into features observed in the data.

DOI: 10.1103/PhysRevB.111.014421

I. INTRODUCTION

Spin-1/2 Heisenberg antiferromagnetic (AFM) chains, in which the local spin environment periodically alternates in orientation, host magnetic properties that dramatically differ from their uniform counterparts. In systems such $Cu(C_6D_5COO)_2 \cdot 3D_2O$ and $Cu(pym)(H_2O)_2(NO_3)_2$ (pym = pyrimidine $C_4H_4N_2$), twofold staggered g tensors and the Dzyalozhinskii-Moriya (DM) interaction result in a staggered internal field perpendicular to the applied field, leading to a field-induced spin gap [1–4]. This is in contrast to the gapless excitation spectra observed in conventional linear chains. The sine-Gordon model of quantum-field theory reproduces the staggered chain's excitation spectrum, which contains soliton and breather modes, plus a $\sim H^{2/3}$ field dependence of its energy gap [5,6].

Despite such unique phenomena displayed by nonlinear $S = 1/2$ chains, investigations into the effects of an alternating spin environment on AFM $S = 1$ chains are notably lacking. In addition to the intra- and interchain energies J_0 and J, the introduction of single-ion anisotropy (SIA) energy D serves as an additional tuning parameter for $S = 1$ systems. When considering a linear chain, the interplay between these parameters results in an already diverse set of possible magnetic ground states [7,8]. In the ideal isotropic, one-dimensional limit, the Haldane gapped phase emerges, which hosts a topologically protected quantum disordered ground state [9]. With easy-plane anisotropy ($D > 0$) as the D/J_0 ratio is increased, the Haldane phase is driven into a quantum paramagnetic phase. Increasing J drives the system into an XY-AFM ordered phase hosting a field-induced BoseEinstein condensation of magnons [10,11]. In the easy-axis ($D < 0$) case, Ising AFM order is induced [8]. Further theoretical efforts have extended this model to explore the effects of rhombohedral anisotropy [12], non-Heisenberg exchange [13], biquadratic exchange [14], and alternating exchange bonds [15].

Here we turn our attention to $Ni(pym)(H_2O)_2(NO_3)_2$, an $S = 1$ analog of the $S = 1/2$ staggered chain; in addition to the aforementioned staggered g tensor, the alternating orientation of local octahedra now presents the possibility of a periodically alternating SIA axis. The alternating SIA, which lacks a global axis in these systems, is expected to act in competition with the exchange interaction. While a staggered SIA axis has attracted attention in the study of Glauber dynamics [16,17] and domain-wall dynamics [18] in single-chain magnets, the ground state of quantum spin-chains with a staggered SIA axis does not appear to have been well explored theoretically or experimentally. In $[Ni(\mu N_3(bmdt)(N_2]_n(DMF)_n$ (bmdt =N,N'-bis(4-methoxylbenzyl)-diethylenetriamine, DMF =N,N-dimethylformamide), weak ferromagnetism and unusual spin dynamics were reported. However, neutron scattering data were not available to solve the magnetic structure or determine the spin Hamiltonian [19]. In three-dimensional and quasi-two-dimensional systems, an alternating easy-axis SIA direction has been found to induce large canting angles and drive weak ferromagnetism, which is normally caused by the DM interaction alone [20,21]. In contrast, in the alternating easy-plane case, collinear order along a pseudo-easy axis created by the intersection of the two local easy planes is found [21,22]. A canted low-temperature magnetic structure might be expected to occur in our Ni staggered chain, with the mean-field canting angle dictated by D/J_0. However, the low-temperature magnetic properties here are likely to be influenced by quantum fluctuations due to the reduced dimensionality and low spin quantum number.

While these systems pose an interesting physical problem, the scarcity of suitably large single crystals and the comparable sizes of D and J_0, are known, from the study of linear $S = 1$ chains, to complicate the full characterization of the Hamiltonian parameters [23,24]. To overcome this, we follow a similar experimental protocol to that highlighted in Ref [23]. We first use x-ray diffraction on small single crystals to determine the crystal structure and infer a magnetic Hamiltonian of the system. Magnetometry measurements on polycrystalline samples are used to confirm the quasi-low-dimensional nature of the interactions and easy-axis anisotropy. Muon-spin relaxation measurements find that the staggered chain undergoes long-range order below $T_N = 2.2$K. While powder neutron diffraction suggests a colinear magnetic ordering, the noise floor of the data leaves room for a large canting angle of up to 25°. Based on the constraints set on the Hamiltonian parameters by the magnetic structure, inelastic neutron scattering (INS) experiments were used to quantify these parameters which are then confirmed using Monte Carlo (MC) simulation of the powder-averaged magnetization.

*Contact author: s.vaidya@warwick.ac.uk
†Deceased.
‡Contact author: p.goddard@warwick.ac.uk

2469-9950/2025/111(1)/014421(11) Published by the American Physical Society

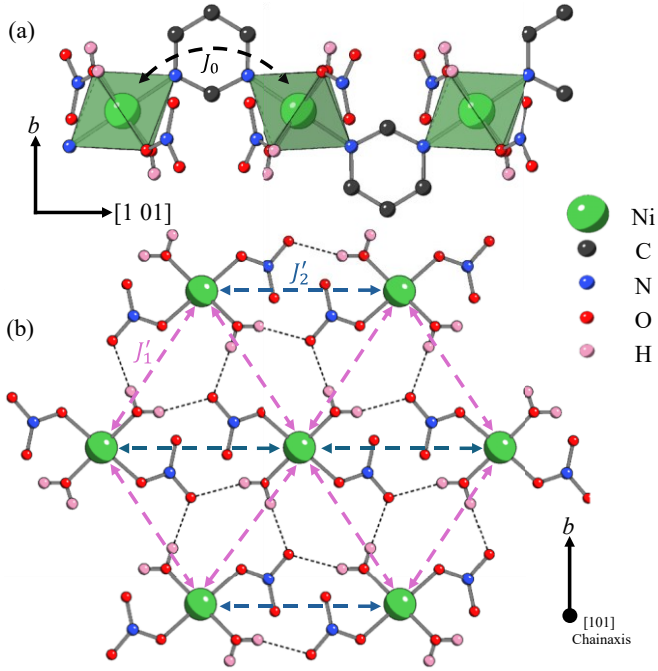

FIG. 1. (a) The chain structure of $Ni(pym)(H_2O)_2(NO_3)_2$ (pym=pyrimidine) determined using single-crystal x-ray diffraction at $T = 300$K. For clarity, $(101)^{-}$ *hkl* plane with only a single chain running along the [101] direction is depicted. (b) View along the [101] axis showing the hydrogen bond network connecting Ni(II) ions in adjacent chains. The purple and blue dashed arrows highlight the two types of inequivalent interchain exchange bonds J_1' and J_2. Each ion has six interchain neighbors.

II. RESULTS AND DISCUSSION

A. X-ray diffraction

Single crystal x-ray diffraction (XRD) was used to determine the crystal structure of the staggered chain, $Ni(pym)(H_2O)_2(NO_3)_2$, at 300 K with the structure shown in Fig. 1. To minimize absorption corrections, small (sub mm) single crystals are preferred for these experiments. For our measurements we used a sample with dimensions $0.23 \times 0.19 \times 0.05$ mm^3. Further details of the synthesis methods, single crystal XRD and structural refinement are provided in the Supplemental Material [25]. Samples crystallize in the monoclinic space-group $C2/c$, with lattice parameters, a = 12.7376(3) Å, b = 11.4975(3) Å, c = 7.3884(2) Å, and β = 115.535(1)°. There are four Ni(II) ions residing at [1/4 1/4 1/2], [1/4 3/4 0], [3/4 3/4 1/2] and [3/4 1/4 0] positions in the unit cell. The octahedra of each Ni(II) ion include equatorial coordination to four O donor atoms from the H_2O and NO_3 ligands at distances 2.065 and 2.085 Å, respectively, and axial coordination to N atoms from the pym ligands that bridge two Ni(II) ions related by a translation of [1/2 0 1/2]. Consequently, chains of Ni-pym-Ni lie along the crystallographic [1 0 1] direction. However, due to the position of the N atoms in the aromatic pym ring, the octahedra of each Ni(II) ion are tilted out of the chain axis towards the b axis by an angle $\alpha = 33.88(4)°$, leading to a twofold staggering of the Ni(II) octahedra as shown in Fig. 1(a). From the structure, it is evident that any SIA present will result in the local N-Ni-N axis defining either the easy axes or the normal to the easy planes. Furthermore, the slight difference in the coordinate bonds to the two different ligand species (H_2O and NO_3) in the equatorial plane suggests the possibility of a small rhombohedral anisotropy with energy E.

The hydrogen-bond networks illustrated in Fig. 1(b) stabilize the interchain structure. Each magnetic ion has six neighbors in adjacent chains; two neighbors residing at a distance of 7.388 Å along the c axis, and four neighbors with distance 6.833 Å along the unit cell diagonals. Consequently, two possible interchain exchange interactions exist, J_1 along the [0,1,1] and [0,1¯,1] directions and J_2 along c axis. These exchange pathways, depicted as purple and blue dashed arrows respectively in Fig. 1(b), constitute a hexagonal lattice in the interchain directions. If $J_2' > 0$ (AFM), this triangular arrangement of the interchain spins will result in competition between the J_1 and J_2 interactions.

The Hamiltonian of the staggered chain can be written as

$$\mathcal{H} = J_0 \sum_i \hat{\mathbf{S}}_i \cdot \hat{\mathbf{S}}_{i+1} + \sum_{\langle i,j\rangle_\perp} J'_{ij} \hat{\mathbf{S}}_i \cdot \hat{\mathbf{S}}_j + \sum_i \hat{\mathbf{S}}_i \cdot K_i \cdot \hat{\mathbf{S}}_i + \sum_i \mu_B \mu_0 g \mathbf{H} \cdot \hat{\mathbf{S}}_i, \quad (1)$$

where $\hat{\mathbf{S}}_i$ is the spin of ion i. Here, the first sum is over the nearest neighbors along the Ni-pym chain with interaction strength J_0 and the second sum is over unique interchain exchange bonds $\langle i, j\rangle_\perp$. The third term describes the SIA with the local anisotropy tensors K_i in the xyz laboratory frame. In the local frame of Ni(II) ions, the anisotropy tensor K_i^{loc} = diag$[E,-E,D]$ and Euler rotations are used to transform K_i^{loc} to K_i, as shown in Ref. [25]. The final term is the Zeeman energy with an applied field $\mu_0\mathbf{H}$ and an isotropic g factor. In reality, we expect a small g anisotropy of magnitude $g = g_z - g_{xy} = 2D/\lambda$, where $\lambda \sim 500$K is a typical value of the spin-orbit coupling parameter for Ni(II) ions in octahedral environments [26]. This would result in a staggered g tensor and an internal staggered field with components perpendicular to the applied field. However, nonstaggered Ni(II) systems with local environments similar to this material typically exhibit SIA energies on the order of $D \sim$ 10K [27], resulting in a very small $g \sim 0.04$, which is an order of magnitude smaller than seen in the Cu(II) staggered chains [1,2].

C2/c is a centrosymmetric space group, with the Ni ions located on inversion centres, while the nearest-neighbor exchange bonds are not centrosymmetric. This permits a DM interaction which changes sign from one bond to the next and has the form $(-1)^i \mathbf{D}_{DM} \cdot \mathbf{S}_i \times \mathbf{S}_{i+1}$. However, in molecule-based

Ni(II) systems, where the spin-orbit coupling is relatively weak, the magnitude of the DM vector, $\mathbf{D}_{DM}$, is expected to be small in comparison to the dominant interaction terms described in Eq. (1) [21,22,28].

B. Magnetometry

Figure 2 presents the zero-field-cooled (ZFC) magnetic susceptibility $\chi(T)$ data for powder samples of the staggered chain, $Ni(pym)(H_2O)_2(NO_3)_2$. The field-cooled $\chi(T)$ was found to coincide with the ZFC curve. For 75 T 300K, $\chi(T)$ is well described by the Curie-Weiss (CW) law, $\chi(T) =$

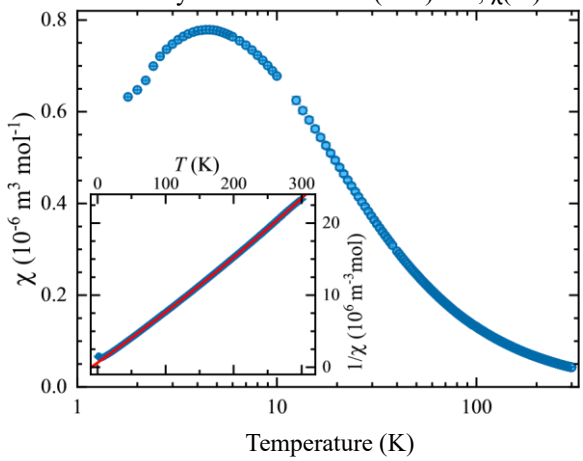

FIG. 2. Temperature dependence of the zero-field-cooled (ZFC) magnetic susceptibility χ (blue circles) of the staggered $S = 1$ chain $Ni(pym)(H_2O)_2(NO_3)_2$, measured in an applied field of 0.1 T. The field-cooled curve coincides with the ZFC. (Inset) Data plotted as the inverse magnetic susceptibility χ^{-1} with a Curie-Weiss fit (red line).

$C/(T - \theta_{CW}) + \chi_0$, where χ_0 is a temperature independent term, the Curie constant $C = N_A\mu_0 g^2\mu_B^2 S(S+1)/3k_B$ and θ_{CW} is the Curie-Weiss temperature. Fitting to χ^{-1}, as shown in the inset to Fig. 2, gives $g = 2.18(1)$, $\chi_0 = -5.49(7) \times 10^{-9}$ m^3 mol^{-1} and $\theta_{CW} = -9.3(2)$K. The g factor is typical of Ni(II) spin-1 systems, whereas the negative θ_{CW} is indicative of AFM coupling between Ni(II) ions. On cooling below 75 K, the data depart from the CW behavior and develop a broad hump centered at around $T_{\chi max} = 4.5(1)$K, which is characteristic of quasi-low-dimensional systems and is due to the buildup of short-range correlations along the chain.

Figures 3(a) and 3(b), respectively, present the pulsed-field magnetization, $M(H)$ curve and the differential susceptibility dM/dH of powder samples at various temperatures. At the lowest temperature of 0.59 K, a sharp peak in dM/dH, corresponding to an upturn in magnetization, is observed at $\mu_0 H_{SF} = 4.1(1)$T. We ascribe this feature to a spin-flop transition commonly observed in systems with easy-axis anisotropy. The transition is no longer present for T 4.08K, indicating long-range magnetic order is absent at this temperature. Additional satellite peaks are observed at 3.3(1) and 6.7(2) T, which are broadened and no longer visible as peaks at 1.58 K. Increasing the field further results in a concave rise up to the projected magnetization saturation value of $m = 2.06$ μ_B per ion, suggesting a low-temperature $g = 2.06(1)$. The $M(H)$ features and the Monte Carlo simulation are discussed in detail in Sec. IIF.

C. Muon-spin relaxation

In order to probe the magnetic transition, zero-field muon-spin relaxation (ZF μ^+SR) measurements were performed on powder samples of $Ni(pym)(H_2O)_2(NO_3)_2$, down to $T = 0.28$K, using the Dolly spectrometer at Swiss Muon Source, Paul Scherrer Institut. No oscillations are observed in the measured ZF spectra at any temperature; instead the spectra show rapid relaxation at low temperatures [Fig. 4(a)]. At temperatures $T >$ 5K, the spectra

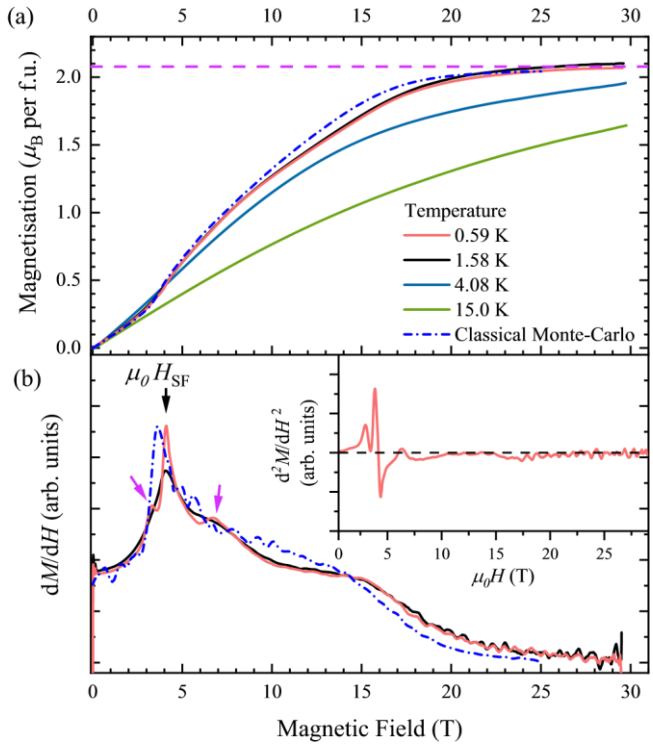

FIG. 3. (a) Magnetization M vs applied magnetic field $\mu_0 H$ for powder samples of the staggered $S = 1$ chain $Ni(pym)(H_2O)_2(NO_3)_2$ at various temperatures. The purple dashed line shows the 0.59 K magnetic saturation at 2.06 μ_B per ion. (b) Differential susceptibility dM/dH vs $\mu_0 H$. The black arrow indicates the spin-flop transition seen as a peak in dM/dH. The purple arrows highlight the additional peaks observed in the 0.59 K data. The blue dash-dot line in both shows the results of a classical Monte Carlo simulation. (Inset) d^2M/dH^2 at 0.59 K.

show a more gradual Gaussian relaxation, typically reflecting disordered electronic moments fluctuating too rapidly to relax the muon spins, leaving the muons to be depolarized by the quasistatic, disordered nuclear spins [29]. This is strongly suggestive of a magnetic ordering transition taking place between these limits in T. To capture the change in the spectra, data were fitted to the phenomenological function

$$A(t) = A_1 e^{-(\lambda t)^\beta} + A_2. \quad (2)$$

Here β accounts for the evolving shape of the spectra and λ parameterizes the relaxation rate. The results of the fitting procedure are shown in Figs. 4(b) and 4(c).

We see a sharply-defined change in the shape of the spectra and a rapid fall in λ on warming from base temperature, consistent with the onset of long-range magnetic order at $T_N = 2.3$K. This also coincides with the end of the rapid fall in λ. (At low T in the presence of dynamic relaxation, λ should be expected to vary with the square of the localν fluctuating magnetic field, such that λ gives us a measure of the order

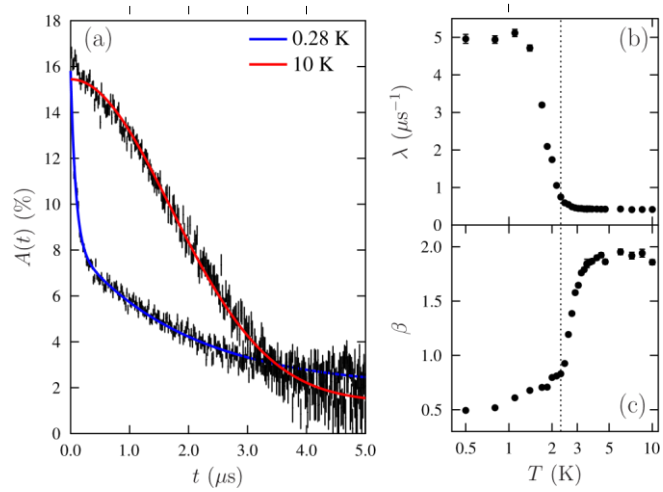

parameter, assuming no change in fluctuation rate close to the transition [29]).

We note that the presence of a rapid relaxation in the muon spectra for $T < T_N$, rather than oscillations, was also

FIG. 4. (a) Representative ZF μ^+SR spectra measured above and below the magnetic transition at 2.3 K. (b) Relaxation rate and (c) shape parameter extracted from fits to Eq. (2). The estimated transition temperature, $T_N = 2.3$K, is shown with a dotted line.

observed in related Ni(II)-based systems such as the series $NiX_2(pyz)_2$ [30], while oscillations are observed below T_N in other molecule-based systems, such as $Ni(NCS)_2(thiourea)_2$ [31]. Here, the absence of oscillations points to an increased level of magnetic disorder (compared to those cases where oscillations are observed), or to fast magnetic fluctuations on the muon timescale with a fluctuation rate $\nu > \gamma_\mu B_{int}$, where B_{int} is the characteristic internal magnetic field at the muon site and γ_μ is the muon gyromagnetic ratio [29].

D. Elastic neutron diffraction

Elastic neutron diffraction measurements were performed on the WISH instrument at ISIS, the UK Neutron and Muon Source [32]. Data were collected on partially deuterated powder sample of $Ni(pym)(D_2O)_2(NO_3)_2$, where H_2O was substituted by D_2O. The magnetic properties were found to be very similar to the hydrogenated sample based on our $\chi(T)$ measurements. A quantitative Rietveld refinement of the crystal structure, conducted using FULLPROF [33], is shown in Fig. 5(a) and reveals that the deuterated sample retains the $C2/c$ structure of the hydrogenated samples down to 0.28 K. The resulting lattice parameters, a = 12.7441(3) Å, b = 11.4933(4) Å, c = 7.3871(2) Å, and β = 115.488(3)°, are in close agreement with values obtained using x-ray measurements on the hydrogenated samples and the small differences are attributed to deuteration. At 2.08 Å and below, there are several additional high-intensity peaks modelled by a LeBail fit of a $Fm\bar{3}m$ copper structure. These peaks arise from the copper sample holder and a thin copper wire within

the sample space required for cooling. Further details of the structural refinement are given in the Supplemental Material [25].

Subtracting the neutron diffraction data collected at 5 K from the data collected at 0.28 K reveals several additional peaks due to the long-range ordered magnetic structure [Fig. 5(b)]. Indexing these peaks reveals a commensurate magnetic propagation vector $\mathbf{k} = (1/2,1/2,1/2)$. The

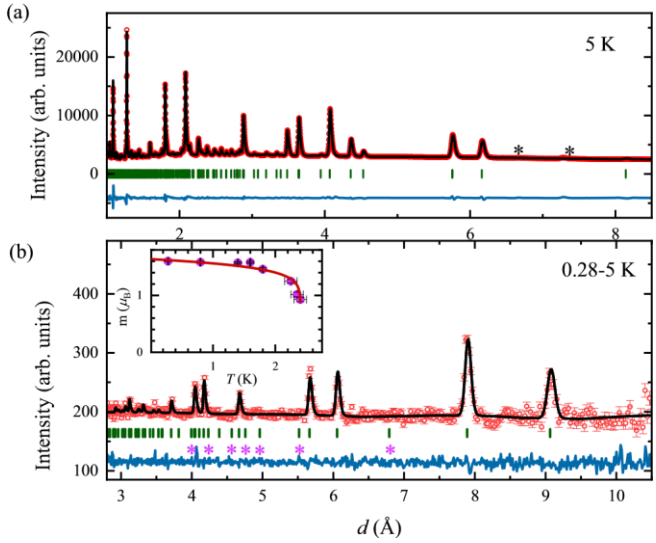

FIG. 5. Neutron powder diffraction data (red circles) of the staggered $S = 1$ chain $Ni(pym)(D_2O)_2(NO_3)_2$. Fits are shown as solid black lines, vertical tick marks show the Bragg positions and solid blue lines indicate the difference curves. (a) Rietveld refinement of the $C2/c$ nuclear structure at $T = 5$K in addition to a LeBail fit of a copper $Fm\bar{3}m$ phase. The black stars mark low-intensity impurity peaks. (b) The magnetic diffraction pattern, obtained by subtracting the nuclear and impurity peaks of the $T = 5$K data from data collected at $T = 0.28$K. Purple stars mark the ferromagnetic satellites of the $h + l = 2n + 1$ Bragg positions which are discussed in the text but are absent in the data. (Inset) T dependence of the ordered Ni(II) magnetic moment.

observed magnetic peaks are satellites of the $h + k = 2n$ reflection allowed by c-centering. The projection of the centering vector, [1/2,1/2,0], on $\mathbf{k}$ yields a phase factor of $e^{i\pi} = -1$ on the moments of sites related by c-centering. Hence, the sites related by c centering are aligned antiparallel. Symmetry analysis using ISODISTORT [34,35] reveals only one candidate symmetry (irrep mL_1^+) for the magnetic structure. Within this irreducible representation, the spins in the unit cell connected by pym (not related by c-centering) are symmetrically inequivalent magnetic sites and are not constrained by symmetry. The moments of these two spins can be decomposed into a linear combination of orthogonal ferromagnetic (FM), $\mathbf{m}_{FM}$, and AFM, $\mathbf{m}_{AFM}$, modes:

$$\mathbf{m}_1 = \mathbf{m}_{FM} + \mathbf{m}_{AFM}, \quad (3)$$

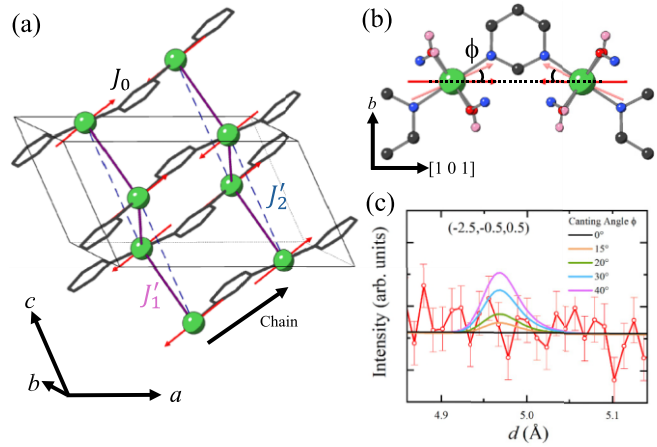

$$\mathbf{m}_2 = \mathbf{m}_{FM} - \mathbf{m}_{AFM}. \quad (4)$$

As shown by the magnetic scattering intensity calculations in the Supplemental Material, $\mathbf{m}_{FM}$ and $\mathbf{m}_{AFM}$ can only contribute to the satellites of $h + l = 2n + 1$ and $h + l = 2n$ peaks respectively [25]. Only the AFM peaks are clearly present in the data of Fig. 5(b), suggesting a solely AFM coupling between spins connected by pym and absence of spin-canting arising from the FM mode. However, simulations of the most intense $h + l = 2n + 1$ satellite peak,

$(-5/2,-1/2,1/2)$, in Fig. 6(c) show that for canting angles $\phi \leqslant 25^\circ$, these peaks would not be visible above the noise floor of the data. The magnetic refinement was carried out with a fixed $\phi = 0$.

FIG. 6. (a) The collinear magnetic structure of $Ni(pym)(D_2O)_2(NO_3)_2$, suggested by powder neutron diffraction measurements. The red arrows indicate the Ni(II) magnetic moment vectors. lines between ions highlights the three exchange interactions: J_0 through the pym ligand, J_1 (solid purple lines) and J_2 (blue dashed lines). The solid black line shows the monoclinic structural unit cell boundary. (b) View of the $(1\ 0\ 1)^-$ hkl plane. The pink arrows show the spin-canting at angle ϕ, expected to be induced by a staggered easy-axis anisotropy direction. (c) Simulation of the $(-5/2,-1/2,1/2)$ neutron diffraction peak for various canting angles with the observed data in red.

The refined magnetic structure is presented in Figs. 6(a) and 6(b). Spins lie collinearly in the ac plane at an angle, $\theta = 48(1)^\circ$ away from the a axis. This structure indicates easy-axis anisotropy, where θ is expected to be determined by the projection of the local Ni-pym-Ni easy SIA axis onto the ac plane, the rhombohedral anisotropy and a small allowed staggered DM interaction. By contrast, if there was a dominant staggered easy-plane anisotropy, then spins would be expected to align perpendicular to the chain and the b axis, along a pseudo-easy axis defined by the intersection of the two local easy planes [21,22].

If spin canting induced by a staggered easy-axis SIA were present, the spins would rotate away from the ac plane, towards the easy axes (local Ni-N axis) at an angle of ϕ as

depicted in Fig. 6(b). Considering a minimal mean-field model containing only J_0 and D energy scales, the derivation presented in the Supplemental Material [25] yields the expression:

$$|D| = \frac{-\sin(2\phi)}{J_0 \sin(\phi - \alpha)\cos(\phi - \alpha)}. \quad (5)$$

The $\phi \leqslant 25°$ limit of the data and Eq. (5) set an upper limit on the ratio $|D|/J_0 \leqslant 4.7$.

Constraints on J_1' and J_2' are determined by the observed interchain order. Spins connected by the J_2 exchange bond along the c-axis exhibit AFM order, which requires that $J_2' > 0$ and $|J_2'| > |J_1'|$ (i.e., J_2 must be AFM and stronger than J_1 for AFM order along c). If $|J_2'| < |J_1'|$, FM order along c is imposed by the stronger J_1' interaction and if $J_2' < 0$, there is no competition between J_1 and J_2' leading to FM order along c. In our system, the competition between J_1' and J_2', is related to the formation of two **k** domains, **k** = (1/2,1/2,1/2) and (−1/2,1/2,1/2). Depending on the choice of the **k** domains, we find that the spins linked by the J_1 exchange bonds exhibit either AFM or FM order along [0,1,1] and FM or AFM order along [0,1¯,1].

The temperature dependence of the low-temperature zerofield ordered Ni(II) moment, m, is shown in the inset to Fig. 5(b). Below $T = 1.6$K, m reaches a constant value of 1.6(1) μ_B. The suppression of the moment size, from the classical expectation value of $gS \approx 2.06$ μ_B, as seen at high-field, is indicative of the effect of quantum fluctuations. Additionally, the sharp change in m at T_N, is as expected for low dimensional systems [36,37]. A fit to a power-law of the form $m(T) = m(0)(1 - T/T_N)^{\delta}$ yields $m(0) = 1.64(3)$ μ_B, $\delta = 0.08(2)$, and $T_N = 2.40(2)$K, in good agreement with the magnetic ordering temperature determined through μSR measurements. Sparseness of the data points around T_c, where the critical exponent δ is most sensitive, means that the critical exponent δ extracted from this fit should not be used to give a tight constraint on theoretical models.

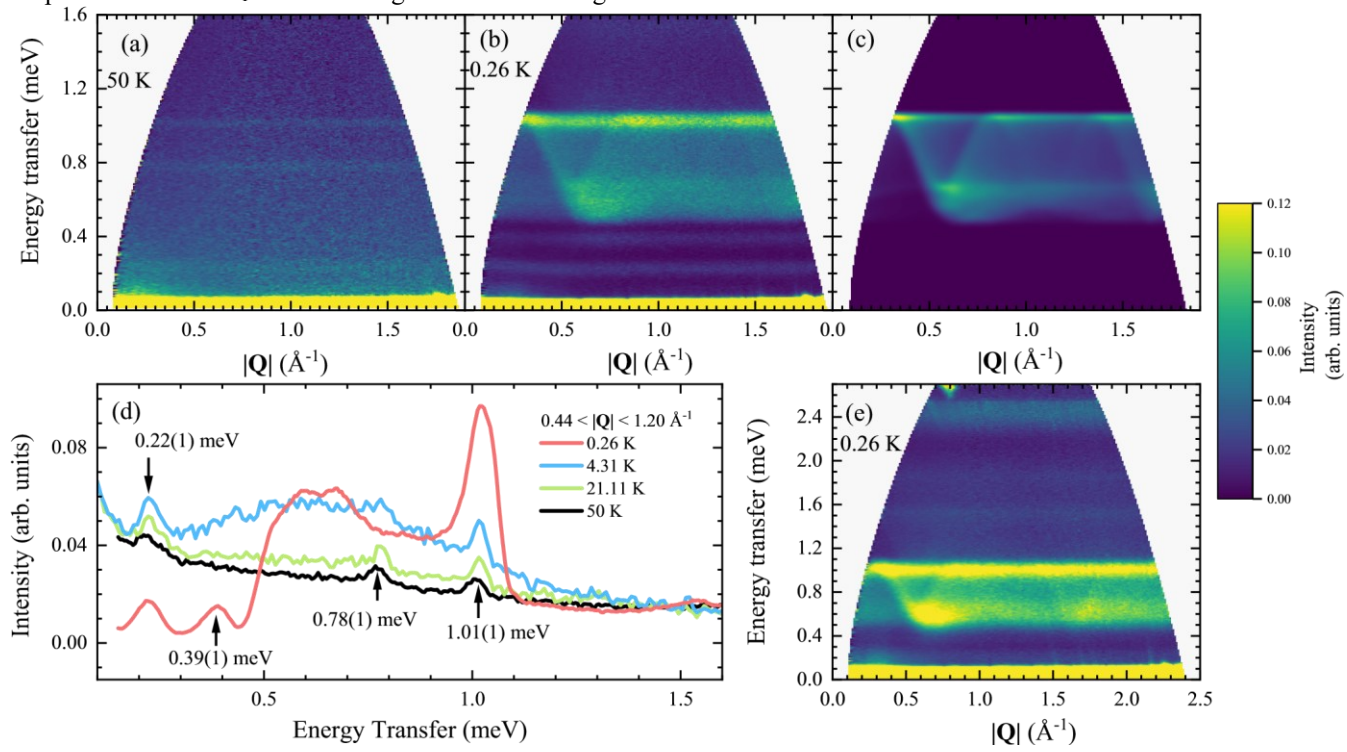

FIG. 7. Time-of-flight inelastic neutron scattering (INS) spectra measurement of powder Ni(pym)$(D_2O)_2(NO_3)_2$ with $_i = 2.04$meV at (a) $T = 50$ and (b) 0.26 K. (c) Powder average liner-spin-wave-theory simulation of the spin-wave spectra using Eq. (1) and the parameters: $J_0$0.18(3)K, and single-ion-anisotropy with an easy-axis component $D = -2.79(1)$K and a rhombohedral component $E = 0.19(9)$K. (d) Temperature dependence of the neutron scattering intensity as a function of the energy transfer for Ni(pym)$(H_2O)_2(NO_3)_2$. The intensity here has been integrated over moment transfer 0. . (e) INS spectra collected at $T = 0.25$K with $_i = 3.36$meV.

$= 5.107(7)\,\mathrm{K}, J_1' = 0.00(5)\,\mathrm{K}, J_2' =$

E. Inelastic neutron scattering

To quantify the sizes of the exchange interactions and anisotropy energies present in Ni(pym)$(DO_2)_3(NO_3)_2$, INS measurements were performed on the partially deuterated powder samples on the LET instrument at ISIS with incident

$44 \leqslant |\mathbf{Q}| \leqslant 1.20$ Å^{-1}

energies $_i$ = 2.04 and 3.36 meV. LET is a multiplexing spectrometer which allows simultaneous measurements with different neutron incident energies. This allows us to survey a wide range of energy while maintaining high resolution at low energies. Further details are provided in Refs. [38–40]. Figures 7(a) and 7(b) present the spectra collected at T = 50 and 0.26 K respectively with incident energy $_i$ = 2.04meV. We note that additional measurements were performed at T = 4.31 and 21.11 K using high-resolution chopper settings, whilst the T = 50 and 0.26 K measurements used high flux chopper settings. This results in an intensity scaling factor of ≈ 3.1 which we obtained from calculations of the chopper opening times and verified by comparing the intensities of the nuclear (220) peak. In any case, the spectral features have widths ≈ 0.1 meV, which are considerably broader than the full width at half maximum (FWHM) resolution of either the high-resolution (0.035 meV) or high-flux (0.06 meV at the elastic line) modes, such that the datasets may be compared.

In the paramagnetic phase at 50 K, three dispersionless features are observed at neutron energy transfers of = 0.22(1), 0.78(1), and 1.01(1) meV. The momentum integrated energy cuts, at various temperatures, shown in Fig. 7(d), reveal that the 0.78 meV excitation diminishes in intensity on cooling and is attributed to localized vibrational modes. In contrast, the 0.22 meV peak grows in intensity on cooling down to 0.25 K, implying it arises from a localized spin excitation from a ground state whose population increases on cooling.

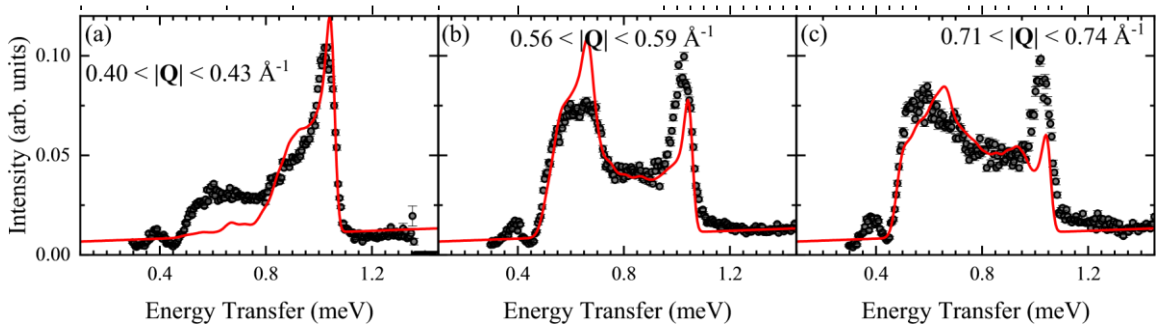

FIG. 8. Inelastic neutron scattering intensity of the staggered $S = 1$ chain $71 \leqslant |\mathbf{Q}| \leqslant 0.74$ Å^{-1} $\mathrm{Ni(pym)(D_2O)_2(NO_3)_2}$ as a function of the energy transfer, integrated over (a) $0.40 \leqslant |\mathbf{Q}| \leqslant 0.43$ Å^{-1}, (b) 0.56 $|\mathbf{Q}|$ 0.59 Å^{-1} and (c) 0.. The data are shown as black circles

and the red lines show the fits to the data discussed in the text.

In this powder sample, this excitation could originate from the transition between the SIA split singlet $|m_s = 0\rangle$ and doublet $|m_s = \pm 1\rangle$ states of Ni(II) ions in an octahedral environment orphaned from the exchange network due to defects or chain ends. This would point to a SIA energy of $|D| = 2.6(1)$K. The 1.01 meV peak also grows in intensity on cooling and coincides with the large peak corresponding to the top of the spin-wave excitation band in the ordered phase.

Data collected in the ordered phase ($T = 0.26$K) mark the emergence of dispersive spin-wave excitations along with a dispersionless in-gap excitation at 0.39(1) meV [Fig. 7(b)]. Additionally, in the $_i = 3.36$meV data shown in Fig. 7(e), we observe low-intensity double-magnon scattering that extends to 1.8(2) meV, approximately twice the value of the single-magnon excitation maximum, along with another dispersionless feature at 1.52(2) meV. The spin-wave excitations were analyzed using the Hamiltonian in Eq. (1) and linear spin wave theory (LSWT), as implemented in the SPINW [41] program and taking the ground state from elastic neutron diffraction measurements. The SIA parameters used in SPINW simulations here were renormalized by a factor $[1 - 1/(2S)]$ to account for the nonlinear contributions to the SIA which are omitted in LSWT [42,43].

Sharp dispersive features are observed in the data, extending from the energy gap of 0.46 meV and 0.69 Å^{-1} (magnetic Bragg position) to the top of the band at 1.02(1) meV. Simulations using Eq. (1) indicate that the energy gap is predominantly governed by D and increases with a larger D. Conversely, the bandwidth of the sharp dispersive feature narrows as D increases and broadens with larger J_0. Reproducing the excitation gap, bandwidth and the sharp dispersion lines observed in the data allows us to accurately determine a unique set of values for D and J_0, which are later refined against the data.

Within the 0.46 0.76meV region, there is an accumulation of spectral weight and a periodic modulation of the energy gap as a function of $|\mathbf{Q}|$. This suggests that intensity in this region arises from dispersive spin-wave branches that are broadened in and $|\mathbf{Q}|$ by powder averaging. Indeed, we find that interchain spin-wave dispersions in the plane

perpendicular to the chain are contained within this region. As such, increasing values of J_2 increases the width of this band and the modulation of the gap as a function of $|\mathbf{Q}|$. Adding the J_1' term results in the dispersion of the top of this band at 0.76 meV, which appears to be flat in our data, suggesting J_1 is small. These features are well reproduced in our simulations, using estimated values of $J_2' \approx 0.18(3)$K and $J_1' \approx 0.00(5)$K. Simulations of the powder-average spin-wave spectra with different values of J_1 and J_2 are shown in the Supplemental Material [25]. Inspection of the energy cut in Fig. 7(d), reveals a broad feature in this region with two peaks at 0.60(2) and 0.66(2) meV, which was found to originate from to the rhombohedral anisotropy E.

The Levenberg-Marquardt (LM) algorithm was used to optimize J_0, D, and E using seven $|\mathbf{Q}|$ integrated energy cuts, three of which are shown in Fig. 8. Due to the differences in observed and simulated intensities discussed below, further optimization of J_1 and J_2 was not possible and they were fixed to values estimated above.[1] The resulting fitted parameters are $J_0 = 5.107(7)$K (0.4401(6) meV), $D = -2.79(1)$K (0.2412(1) meV) and $E = 0.19(9)$K (0.016(8) meV) and the simulation is depicted in Fig. 7(c). The value of D obtained through fitting the spin-wave spectra is in excellent agreement with the value suggested by the 0.22 meV dispersionless excitation and

[1] When allowed to freely refine during the LM fitting, J_1 and J_2 approach 0 K and $|\mathbf{Q}|$-dependant modulation of the gap is no longer present in the simulations as shown in Ref. [25].

further supports the presence of localized excitations from orphaned Ni(II) ions as proposed earlier. Using Eq. (5) and the fitted $|D|/J_0 = 0.546(3)$, we estimate an canting angle $\phi \approx 6.5^\circ$. This canting is within the limit set by the noise floor of our elastic neutron diffraction data and is not expected to be discernible in those data. The AFM coupling causes spins in neighboring chains to cant in opposite directions, canceling the ferromagnetic component of a single chain. As a result, although spin canting is present in these systems, a zero-field remanent magnetization is not expected, consistent with our powder $M(H)$ data. Additionally, the quasi-one-dimensional nature of our system, implied by our $\chi(T)$, *mu*SR and T-dependent neutron diffraction results, is confirmed by the ratio $J_2'/J_0 \approx 0.04(2)$.

While the form of the observed spectra is captured very well by our model, there are differences in the observed and calculated intensities. This is most pronounced in the $0.46 \leqslant \epsilon \leqslant 0.76$meV region in the energy cut integrated over $0.40 \leqslant |\mathbf{Q}| \leqslant 0.43$ Å^{-1} [Fig. 8(a)], which is dominated by the spin-wave dispersions in the plane perpendicular to the chain. Increased intensity observed in this region suggests a redistribution in the spectral weight from the spin-wave modes along the chain to the interchain modes. This may be attributed to the preferential orientation of the grains in the powder samples such that the interchain scattering plane is more exposed to the neutron beam. Additionally, because LSWT does not account for impurity effects, the 0.22 meV feature is not reproduced in our simulation. We also note that the 0.39 meV in-gap modes were not reproduced in the SPINW simulations, even when higher-order interactions are included, and could hint at a localized excitation mode which LSWT does not capture. One possible explanation is that this feature could arise from excitations between energy levels within small orphaned dimers of Ni(II) ions [44]. Other orphaned structures, such as trimers, may also account for the 1.01 meV excitation seen up to 50 K.

F. Monte Carlo simulation of $M(H)$

Monte Carlo simulations of the powder-averaged longitudinal $M(H)$ were performed to confirm the Hamiltonian parameters determined by the INS experiments. At each field, the simulation aims to minimize the total energy of an eightspin cluster, which is calculated using the Eq. (1) and an isotropic $g = 2.06$ that was determined from the $M(H)$ data at $T = 0.59$K. The resulting $M(H)$ and dM/dH simulations are shown as blue dash-dot lines in Fig. 3. The simulations provide an overall good agreement with the observed spin-flop field at $\mu_0 H_{SF} = 4.1(1)$ T and the rounded approach to the saturation at high fields.

Simulations of single-crystal $M(H)$ data with $J_2' = 0$K and $J_2' = 0.18$ K ($J_1' = 0$K in both cases) were performed to assess the effects of interchain interactions on $M(H)$ (see Fig. 9). The $J_2' = 0$K simulations consider only a single isolated spin chain, and as such show a zero-field remanent magnetization, which as explained above, disappears when multiple chains are considered. When the applied field is parallel to the chain [see Fig. 9(a)], a single spin-flop transition occurs for both $J_2' = 0$ and 0.18 K. This transition occurs at $\mu_0 H_{SF} = 4$ T for $J_2' = 0.18$K and corresponds to the main spin-flop feature found in the power average $M(H)$ data shown in Fig. 3.

In Fig. 9(b), where the applied field is parallel to one of the easy-axis directions, there is a single meta-magnetic transition for $J_2' = 0$K and two separate transitions at 3.4 T and 7.6 T when $J_2' = 0.18$K. Similarly, in Fig. 9(c), where the applied field is parallel to the b axis, the octahedra tilting direction, a metamagnetic transition, associated with neighboring chains flipping, is present at 2.2 T only when $J_2' = 0.18$K.

These additional metamagnetic transitions, which appear in the simulations for certain field directions when interchain interactions are considered, may account for the 3.3(1) and 6.7(2) T, satellite features observed in the 0.59 K powderaveraged dM/dH data. In a powder-averaged measurement, a single peak in dM/dH is expected, as indicated by the powder-average MC simulations in Fig. 3. Preferential orientation of the grains during measurements, may result in an increased contribution to dM/dH from these directions and the observation of distinct satellite peaks in our data.

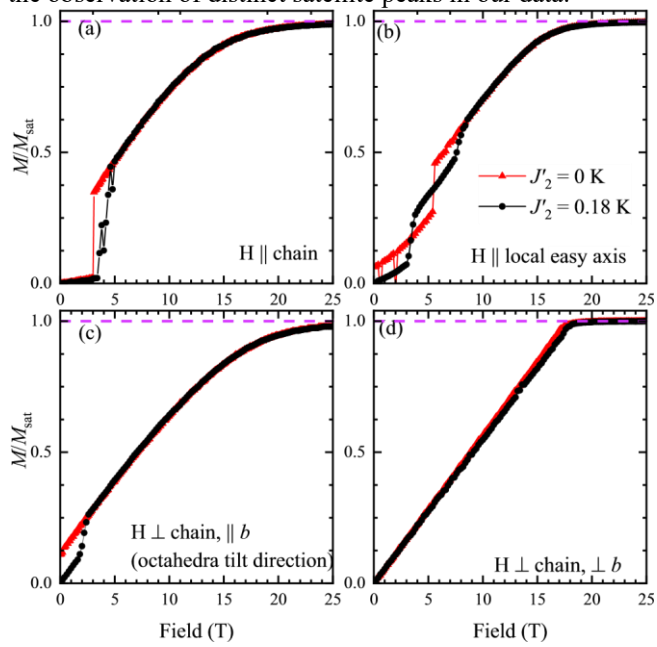

FIG. 9. Monte Carlo simulation of the field-dependent magnetization of the staggered $S = 1$ chain at various field orientations, using Hamiltonian parameters determined using inelastic neutron scattering. The field is applied (a) parallel to the chain, (b) parallel to a local easy axis of a Ni(II) spin, (c) perpendicular to the chain and parallel to the b axis (octahedra tilting direction), and (d) perpendicular to the chain and b (perpendicular

to the plane containing the easy axes). The purple dashed line in all panels indicates magnetic saturation.

In anisotropic magnets, a symmetry-breaking phase transition is often expected to occur at saturation when a large field is applied parallel to the principle anisotropy axis. However, it has been shown recently that in systems with an alternating SIA axis, there are principle directions where the SIA can always save energy by canting spins away from the applied field, and magnetic saturation only occurs in the infinite field limit [22]. Similarly in $Ni(pym)(H_2O)_2(NO_3)_2$, a magnetic saturation phase transition only occurs when the applied field is simultaneously perpendicular to the chain and the b axis [Fig. 9(d)]. This is the direction about which the octahedra rotate and is the only direction where the applied field is perpendicular to both easy axes. For all other field orientations, $M(H)$ asymptotically approaches the saturation value. In the powder-averaged $M(H)$ simulation and data, this is captured by the rounded approach to saturation which shows no features in dM/dH indicative of a phase transition.

III. CONCLUSIONS

We have explored the magnetic properties of a quasione-dimensional $S = 1$ material $Ni(pym)(H_2O)_2(NO_3)_2$. The octahedra of neighboring Ni(II) ions, connected by pym ligands, alternate in orientation leading to a staggered Ni-pym chain. The alternating SIA direction is expected to follow the Ni(II) octahedra. Muon-spin relaxation data show signatures of long-range order below $T_N = 2.3$K, which is stabilized by nonzero interchain interactions. Powder elastic neutron diffraction measurements reveal AFM order and are consistent with a staggered easy-axis anisotropy. In systems with an alternating easy-axis direction, spin canting towards the local easy-axis direction is expected [20,21]. The noise floor of the neutron diffraction data leaves room for spin canting of up to 25°. Powder inelastic neutron scattering experiments were performed to quantify the Hamiltonian. Its parameters, $J_0 = 5.107(7)$ K, $J_1' \approx 0.00(5)$, $J_2' \approx 0.18(3)$K, $D = -2.79(1)$K, and $E = 0.19(9)$K were then determined using INS measurements on powder samples and for the experimentally determined ratio $|D|/J_0 = 0.55(1)$, mean-field calculations show that $\phi \approx 6°$. While our LSWT simulations model the observed dispersive spin-wave excitations well, there are certain features which are not captured. We suggest that some of these features arise from small clusters of Ni(II) spins, such as single ions, dimers and trimers which are orphaned from the chains. Additionally, it has been pointed out elsewhere that some details of $S = 1$ magnetic excitation spectra can only be accounted for generalizing spin-wave modeling to include SU(3) degrees of freedom [45]. This is a developing issue that requires further investigation.

Monte Carlo simulations, using Eq. (1) and the Hamiltonian parameters determined using INS measurements, show that the features in the $M(H)$ are largely accounted for by a classical model and an isotropic g factor. This is in contrast to the $S = 1/2$ staggered chain, where the g anisotropy and the DM interactions have a dramatic effect, mapping the Hamiltonian on to the sine-Gordon model of quantum field theory and giving rise to soliton-like excitation modes [1–6]. Recently, experiments on a chiral $S = 1/2$ system, $[Cu(pym)(H_2O)_4]SiF_6 \cdot H_2O$, hosting a fourfold periodic variation of the spin environments showed behavior which was not governed by the sine-Gordon model [46]. Therefore, exploring a similar extension from the $S = 1$ staggered chain to an $S = 1$ chiral chain could prove interesting.

For a linear $S = 1$ AFM chain with $|D|/J_0 = 0.546(3)$ and $J_{ij}'/J_0 \approx 0.04(2)$, the Haldane phase is already expected to be quenched by D and J into an AFM Ising order [8]. Therefore, to study the robustness of the topological phase in the presence of alternating octahedra and single-ion anisotropy direction, further theoretical studies and the development of real materials close to the quantum critical point are necessary.

ACKNOWLEDGMENTS

We are indebted to the late Jamie Manson for instigating this work, for his role in designing and growing the samples and for many other invaluable contributions. We thank T. Orton and P. Ruddy for their technical assistance. We also thank R. Coldea, D. M. Pajerowski, C. Stock, and J. A. Villa for valuable discussions and B. M. Huddart for his assistance with the muon measurements. S.V. thanks the UK Engineering and Physical Sciences Research Council (EPSRC) for supporting his studentship. This project has received funding from the European Research Council (ERC) under the European Union's Horizon 2020 research and innovation programme (Grant Agreement No. 681260) and EPSRC (Grant No. EP/N024028/1). A portion of this work was performed at the National High Magnetic Field Laboratory, which is supported by National Science Foundation Cooperative Agreements No. DMR-1644779 and No. DMR-2128556, the US Department of Energy (DoE) and the State of Florida. J.S. acknowledges support from the DoE BES FWP "Science of 100 T". S.J.B. was funded by UK Research and Innovation (UKRI) under the UK government's Horizon Europe funding guarantee (Grant No. EP/X025861/1). The authors also thank National Science Foundation (NSF) for funding (NSF CHE1827313). Part of this work was carried out at the Swiss Muon Source, Paul Scherrer Institut and we are grateful for the provision of beamtime (at the Dolly spectrometer). The work at EWU was supported by the National Science Foundation through Grant No. DMR-2104167.

DATA AVAILABILITY

Data presented in this paper will be made available at [52] and the INS data can be found in Refs. [39,40].

[1] D. C. Dender, P. R. Hammar, D. H. Reich, C. Broholm, and G. Aeppli, Direct observation of field-induced incommensurate fluctuations in a one-dimensional S = 1/2 antiferromagnet, Phys. Rev. Lett. **79**, 1750 (1997).

[2] R. Feyerherm, S. Abens, D. Günther, T. Ishida, M. Meißner, M. Meschke, T. Nogami, and M. Steiner, Magnetic-field induced gap and staggered susceptibility in the S = 1/2 chain $[PMCu(NO_3)_2(H_2O)_2]_n$ (PM= pyrimidine), J. Phys.: Condens. Matter **12**, 8495 (2000).

[3] S. A. Zvyagin, A. K. Kolezhuk, J. Krzystek, and R. Feyerherm, Excitation hierarchy of the quantum sine-gordon spin chain in a strong magnetic field, Phys. Rev. Lett. **93**, 027201 (2004).

[4] B. M. Huddart, M. Gomilšek, T. J. Hicken, F. L. Pratt, S. J. Blundell, P. A. Goddard, S. J. Kaech, J. L. Manson, and T. Lancaster, Magnetic order and ballistic spin transport in a sine-Gordon spin chain, Phys. Rev. B **103**, L060405 (2021).

[5] M. Oshikawa and I. Affleck, Field-induced gap in S = 1/2 antiferromagnetic chains, Phys. Rev. Lett. **79**, 2883 (1997).

[6] I. Affleck and M. Oshikawa, Field-induced gap in Cu benzoate and other $S^{=}\frac{1}{2}$ antiferromagnetic chains, Phys. Rev. B **60**, 1038 (1999).

[7] A. F. Albuquerque, C. J. Hamer, and J. Oitmaa, Quantum phase diagram and excitations for the one-dimensional S = 1 Heisenberg antiferromagnet with single-ion anisotropy, Phys. Rev. B **79**, 054412 (2009).

[8] K. Wierschem and P. Sengupta, Quenching the Haldane gap in spin-1 Heisenberg antiferromagnets, Phys. Rev. Lett. **112**, 247203 (2014).

[9] F. D. M. Haldane, Nonlinear field theory of large-spin Heisenberg antiferromagnets: Semiclassically quantized solitons of the one-dimensional easy-Axis Néel State, Phys. Rev. Lett. **50**, 1153 (1983).

[10] V. S. Zapf, D. Zocco, B. R. Hansen, M. Jaime, N. Harrison, C. D. Batista, M. Kenzelmann, C. Niedermayer, A. Lacerda,

and A. Paduan-Filho, Bose-Einstein condensation of $S = 1$ nickel spin degrees of freedom in $NiCl_2{-}4SC(NH_2)_2$, Phys. Rev. Lett. **96**, 077204 (2006).

[11] S. A. Zvyagin, J. Wosnitza, C. D. Batista, M. Tsukamoto, N. Kawashima, J. Krzystek, V. S. Zapf, M. Jaime, N. F. Oliveira, and A. Paduan-Filho, Magnetic excitations in the spin-1 anisotropic Heisenberg antiferromagnetic chain system $NiCl_2{-}4SC(NH_2)_2$, Phys. Rev. Lett. **98**, 047205 (2007).

[12] Y.-C. Tzeng, H. Onishi, T. Okubo, and Y.-J. Kao, Quantum phase transitions driven by rhombic-type single-ion anisotropy in the $S = 1$ Haldane chain, Phys. Rev. B **96**, 060404(R) (2017).

[13] F. Lange, S. Ejima, and H. Fehske, Finite-temperature dynamic structure factor of the spin-1 XXZ chain with single-ion anisotropy, Phys. Rev. B **97**, 060403(R) (2018).

[14] G. De Chiara, M. Lewenstein, and A. Sanpera, Bilinearbiquadratic spin-1 chain undergoing quadratic Zeeman effect, Phys. Rev. B **84**, 054451 (2011).

[15] T. Suzuki and S. I. Suga, Quantized excitation spectra by magnon confinement in quasi-one-dimensional $S = 1$ spin systems, Phys. Rev. B **98**, 180406(R) (2018).

[16] H.-L. Sun, Z.-M. Wang, and S. Gao, Strategies towards singlechain magnets, Coord. Chem. Rev. **254**, 1081 (2010).

[17] W.-X. Zhang, R. Ishikawa, B. Breedlove, and M. Yamashita, Single-chain magnets: Beyond the Glauber model, RSC Adv. **3**, 3772 (2013).

[18] V. Pianet, M. Urdampilleta, T. Colin, R. Clérac, and C. Coulon, Domain walls in single-chain magnets, Phys. Rev. B **96**, 214429 (2017).

[19] X.-T. Liu, X.-Y. Wang, W.-X. Zhang, P. Cui, and S. Gao, Weak ferromagnetism and dynamic magnetic behavior in a single endto-end Azide-Bridged Nickel(II) chain, Adv. Mater. **18**, 2852 (2006).

[20] R. Feyerherm, A. Loose, T. Ishida, T. Nogami, J. Kreitlow, D. Baabe, F. J. Litterst, S. Süllow, H.-H. Klauss, and K. Doll, Weak ferromagnetism with very large canting in a chiral lattice: $Fe(pyrimidine)_2Cl_2$, Phys. Rev. B **69**, 134427 (2004).

[21] J. Pitcairn, M. A. Ongkiko, A. Iliceto, P. J. Speakman, S. Calder, M. J. Cochran, J. A. M. Paddison, C. Liu, S. P. Argent, A. J. Morris, and M. J. Cliffe, Controlling noncollinear ferromagnetism in van der Waals metal–organic magnets, J. Am. Chem. Soc. **146**, 19146 (2024).

[22] S. Vaidya, A. Hernández-Melián, J. P. Tidey, S. P. M. Curley, S. Sharma, P. Manuel, C. Wang, G. L. Hannaford, S. J. Blundell, Z. E. Manson, J. L. Manson, J. Singleton, T. Lancaster, R. D. Johnson, and P. A. Goddard, Pseudo-easy-axis anisotropy in antiferromagnetic $S = 1$ diamond-lattice systems, Phys. Rev. B **110**, 174438 (2024).

[23] J. Brambleby, J. L. Manson, P. A. Goddard, M. B. Stone, R. D. Johnson, P. Manuel, J. A. Villa, C. M. Brown, H. Lu, S. Chikara, V. Zapf, S. H. Lapidus, R. Scatena, P. Macchi, Y. S. Chen, L.-C. Wu, and J. Singleton, Combining microscopic and macroscopic probes to untangle the single-ion anisotropy and exchange energies in an $S = 1$ quantum antiferromagnet, Phys. Rev. B **95**, 134435 (2017).

[24] W. J. Blackmore, J. Brambleby, T. Lancaster, S. J. Clark, R. D. Johnson, J. Singleton, A. Ozarowski, J. A. Schlueter, Y.-S. Chen, A. M. Arif, S. Lapidus, F. Xiao, R. C. Williams, S. J. Blundell, M. J. Pearce, M. R. Lees, P. Manuel, D. Y. Villa, J. A. Villa, J. L. Manson *et al.*, Determining the anisotropy and exchange parameters of polycrystalline spin-1 magnets, New J. Phys. **21**, 093025 (2019).

[25] See Supplemental Material at http://link.aps.org/supplemental/10.1103/PhysRevB.111.014421 for additional details on the experimental methods and sample synthesis. It also includes information on the anisotropy tensor, mean-field and magnetic structure factor calculations, as well as supplementary LSWT calculations and neutron diffraction data, which include Refs. [47–51].

[26] R. Boca, Zero-field splitting in metal complexesˇ , Coord. Chem. Rev. **248**, 757 (2004).

[27] J. L. Manson, Z. E. Manson, A. Sargent, D. Y. Villa, N. L. Etten, W. J. Blackmore, S. P. Curley, R. C. Williams, J. Brambleby, P. A. Goddard, A. Ozarowski, M. N. Wilson, B. M. Huddart, T. Lancaster, R. D. Johnson, S. J. Blundell, J. Bendix, K. A. Wheeler, S. H. Lapidus, F. Xiao *et al.*, Enhancing easy-plane anisotropy in bespoke Ni(II) quantum magnets, Polyhedron **180**, 114379 (2020).

[28] H. Huang and I. Affleck, Susceptibility and DzyaloshinskiiMoriya interaction in the Haldane-gap compound $Ni(C_2H_8N_2)_2NO_2(ClO_4)$, Phys. Rev. B **69**, 184414 (2004).

[29] S. J. Blundell, R. De Renzi, T. Lancaster, and F. L. Pratt, Dynamic effects in magnetism, in *Muon Spectroscopy: An Introduction* (Oxford University Press, Oxford, 2022).

[30] J. Liu, P. A. Goddard, J. Singleton, J. Brambleby, F. Foronda, J. S. Möller, Y. Kohama, S. Ghannadzadeh, A. Ardavan, S. J. Blundell, T. Lancaster, F. Xiao, R. C. Williams, F. L. Pratt, P. J. Baker, K. Wierschem, S. H. Lapidus, K. H. Stone, P. W. Stephens, J. Bendix *et al.*, Antiferromagnetism in a family of $S = 1$ square lattice coordination polymers $NiX_2(pyz)_2$ (X = Cl, Br, I, NCS; pyz = pyrazine), Inorg. Chem. **55**, 3515 (2016).

[31] S. P. M. Curley, R. Scatena, R. C. Williams, P. A. Goddard, P. Macchi, T. J. Hicken, T. Lancaster, F. Xiao, S. J. Blundell, V. Zapf, J. C. Eckert, E. H. Krenkel, J. A. Villa, M. L. Rhodehouse, and J. L. Manson, Magnetic ground state of the one-dimensional ferromagnetic chain compounds $M(NCS)_2(thiourea)_2$ (M = Ni,Co), Phys. Rev. Mater. **5**, 034401 (2021).

[32] L. C. Chapon, P. Manuel, P. G. Radaelli, C. Benson, L. Perrott, S. Ansell, N. J. Rhodes, D. Raspino, D. Duxbury, E. Spill, and J. Norris, Wish: The new powder and single crystal magnetic diffractometer on the second target station, Neutron News **22**, 22 (2011).

[33] J. Rodríguez-Carvajal, Recent advances in magnetic structure determination by neutron powder diffraction, Phys. B: Condens. Matter **192**, 55 (1993).

[34] H. T. Stokes, D. M. Hatch, and B. J. Campbell, ISODISTORT, ISOTROPY Software Suite, https://stokes.byu.edu/iso/isodistort.php.

[35] B. J. Campbell, H. T. Stokes, D. E. Tanner, and D. M. Hatch, *ISODISPLACE*: A web-based tool for exploring structural distortions, J. Appl. Crystallogr. **39**, 607 (2006).

[36] Y. Uemura, A. Keren, L. Le, G. Luke, B. Sternlieb, and W. Wu, Muon spin relaxation studies in frustrated and/or lowdimensional spin systems, Hyperfine Interact. **85**, 133 (1994).

[37] A. Keren, K. Kojima, L. Le, G. Luke, W. Wu, Y. Uemura, S. Tajima, and S. Uchida, Muon-spin-rotation measurements in the 'infinite-chain' Ca_2CuO_3, J. Magn. Magn. Mater. **140–144**, 1641 (1995).

[38] R. Bewley, J. Taylor, and S. Bennington., LET, a cold neutron multi-disk chopper spectrometer at ISIS, Nucl. Instrum. Methods Phys. Res. Sect. A **637**, 128 (2011).

[39] S. Vaidya, S. Sharma, R. Steward, R. Johnson, and P. Goddard, Excitation spectrum in a spin-1 chain with alternating easy-axis direction, STFC ISIS Neutron and Muon Source (2023), https://doi.org/10.5286/ISIS.E.RB2300051.

[40] S. Vaidya, C. Balz, R. Johnson, and P. Goddard, Measuring magnetic anisotropy and magnetic excitation in a staggered spin-1 qntiferromagnetic chain (2023), https://doi.org/10.5286/ISIS.E.RB2390003-1.

[41] S. Toth and B. Lake, Linear spin wave theory for single-Q incommensurate magnetic structures, J. Phys.: Condens. Matter **27**, 166002 (2015).

[42] E. M. Wheeler, R. Coldea, E. Wawrzynska, T. Sörgel,´ M. Jansen, M. M. Koza, J. Taylor, P. Adroguer, and N. Shannon, Spin dynamics of the frustrated easy-axis triangular antiferromagnet 2*H*-$AgNiO_2$ explored by inelastic neutron scattering, Phys. Rev. B **79**, 104421 (2009).

[43] D. Dahlbom, H. Zhang, Z. Laraib, D. M. Pajerowski, K. Barros, and C. Batista, Renormalized classical theory of quantum magnets, arXiv:2304.03874.

[44] S.-H. Lee, C. Broholm, G. Aeppli, T. G. Perring, B. Hessen, and A. Taylor, Isolated spin pairs and two-dimensional magnetism in $SrCr_{9p}Ga_{12-9p}O_{19}$, Phys. Rev. Lett. **76**, 4424 (1996).

[45] X. Bai, S.-S. Zhang, Z. Dun, H. Zhang, Q. Huang, H. Zhou, M. B. Stone, A. I. Kolesnikov, F. Ye, C. D. Batista, and M. Mourigal, Hybridized quadrupolar excitations in the spinanisotropic frustrated magnet FeI_2, Nat. Phys. **17**, 467 (2021). [46] J. Liu, S. Kittaka, R. D. Johnson, T. Lancaster, J. Singleton, T. Sakakibara, Y. Kohama, J. van Tol, A. Ardavan, B. H. Williams, S. J. Blundell, Z. E. Manson, J. L. Manson, and P. A. Goddard, Unconventional field-induced spin gap in an $S = 1/2$ chiral staggered chain, Phys. Rev. Lett. **122**, 057207 (2019).

[47] L. Krause, R. Herbst-Irmer, G. M. Sheldrick, and D. Stalke, Comparison of silver and molybdenum microfocus X-ray sources for single-crystal structure determination, J. Appl. Crystallogr. **48**, 3 (2015).

[48] G. M. Sheldrick, *SHELXT* – Integrated space-group and crystal-structure determination, Acta Crystallogr. Sect. A **71**, 3 (2015).

[49] G. M. Sheldrick, Crystal structure refinement with *SHELXL*, Acta Crystallogr. Sect. C **71**, 3 (2015).

[50] O. V. Dolomanov, L. J. Bourhis, R. J. Gildea, J. A. K. Howard, and H. Puschmann, *OLEX2*: A complete structure solution, refinement and analysis program, J. Appl. Crystallogr. **42**, 339 (2009).

[51] J. Hannay and J. Nye, Fibonacci numerical integration on a sphere, J. Phys. A: Math. Gen. **37**, 11591 (2004).

[52] S. Vaidya *et al.*, Data for "Magnetic properties of a staggered $S = 1$ chain with an alternating single-ion anisotropy direction," [Data set] (2025), https://wrap.warwick.ac.uk/188291/.

Correction: Support information was incomplete and has been fixed.

Second Correction: The first Correction contained an error in the support information that has now been rectified.